Materials and Design 131 (2017) 460–469

Contents lists available at ScienceDirect

Materials and Design

journal homepage: www.elsevier.com/locate/matdes

Spatter formation in selective laser melting process using multi-laser technology

Mohsen Taheri Andani [a], Reza Dehghani [b], Mohammad Reza Karamooz-Ravari [b], Reza Mirzaeifar [c], Jun Ni [a,*]

[a] S.M. Wu Manufacturing Research Center, College of Engineering, Department of Mechanical Engineering, University of Michigan, Ann Arbor, MI 48109, USA
[b] Department of Mechanical Engineering, Graduate University of Advanced Technology, Kerman, Iran
[c] Department of Mechanical Engineering, Virginia Tech, Blacksburg, VA 24061, USA

HIGHLIGHTS

- High-speed photography is utilized to observe the formation mechanism of spatters.
- An image analysis framework is developed to assess the distribution of induced spatters.
- Spatter particles are detrimental type of defects on mechanical properties of SLM parts.

GRAPHICAL ABSTRACT

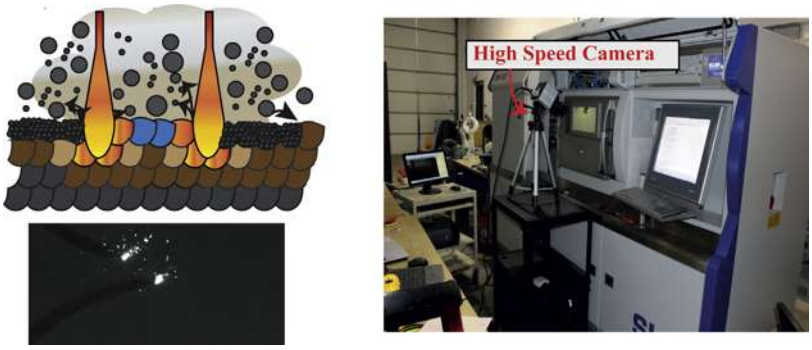

ARTICLE INFO

Article history:
Received 3 May 2017
Received in revised form 30 May 2017
Accepted 16 June 2017
Available online 22 June 2017

Keywords:
Selective laser melting
Spatter particles
Multi-laser technology
High-speed photography
Unmelted region

ABSTRACT

This study demonstrates the significant role of recoil pressure in selective laser melting (SLM) process using multi-laser technology. High-speed photography is utilized to observe the formation mechanism, and also the behavior of spatter particles during SLM fabrication. A computational image analysis framework is developed to assess the size and the number of induced spatters. The morphology and the composition of spatters and their influence on the surface of the fabricated parts are determined. Unmelted regions, resulting from spatter deposition into the powder or the solidified layer, are found to be a detrimental type of defects on mechanical properties of SLM parts. This is followed by a discussion on demand for developing a meaningful process parameters optimization to enhance the mechanical properties of SLM products.

1. Introduction

During the past decades, additive manufacturing (AM), particularly metallic AM, has drawn extensive attention due to its unique ability for layer-by-layer fabricating parts of various complexities [1,2]. Selective laser melting (SLM) as a novel metallic AM process has demonstrated a promising future [3]. The SLM technology allows fabrication of high-density metallic parts (up to 99.9%), exhibiting extremely fine microstructures with very complex geometries that cannot be easily

* Corresponding author at: 3455 GGB (George G. Brown Laboratory), 2350 Hayward, Ann Arbor, MI 48109, USA.
E-mail addresses: mtaheri@umich.edu (M. Taheri Andani), r.dehghani@kgut.ac.ir (R. Dehghani), m.karamooz@kgut.ac.ir (M.R. Karamooz-Ravari), rmirzaei@vt.edu (R. Mirzaeifar), junni@umich.edu (J. Ni).

http://dx.doi.org/10.1016/j.matdes.2017.06.040
0264-1275/

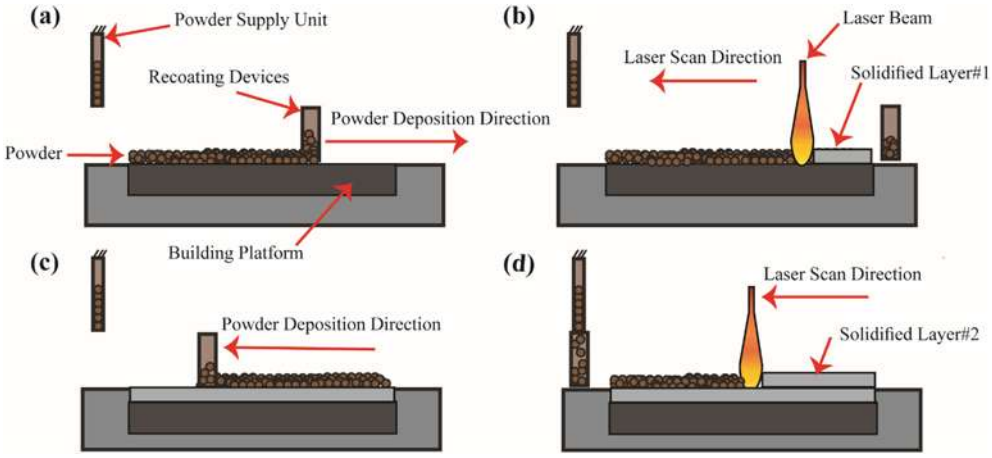

Fig. 1. Schematic representation of the fabricating sequences in SLM 280HL machines. (a) Bi-directional recoating devices deposit the powder on the building platform. (b) The laser beam melts selectively the powder based on the CAD model. (c) The recoating devices deposit the powder on the solidified layer. (d) The laser beam fuses the next layer and the powder supply unit fills the recoating devices.

fabricated by conventional methods [4–9]. However, widespread adoption of SLM with metallic parts depends on whether the final products meet the requirements of engineering quality standards [10]. This includes reducing the defects induced by spatters, which can adversely affect the mechanical properties.

Spatter creation have been reported in several laser-assisted manufacturing works [11–16]. Some examples are the works by Low et al. [11,12] on studying the spatter formation mechanism during laser drilling and the effects of laser process parameters on spatter deposition. However, few research studies have been conducted on spatter creation mechanisms during SLM process. Simonelli et al. [15] studied oxidation reactions during the SLM process and its effect on the spatter composition. They found that the chemical compositions in spatter particles change significantly compared to the initial powder. Khairallah et al. [14] used a three-dimensional high fidelity powder-scale model to study the importance of recoil pressure and Marangoni convection in shaping spatter particle during laser bed-fusion process. Mumtaz and Hopkinson [16] used a pulse shaping technique to control the heat delivered to the laser-material interaction zone and consequently reduce the amount of induced spatter during SLM process. In another study spatter creation mechanism has been observed in single track experiments by employing 316 stainless steel powder [17]. The authors found that laser energy input affects the size, scattering state and jetting height of spatter significantly. Despite these studies on SLM technique, there is still a gap of knowledge and obvious need for a systematic analysis of spatter creation during SLM process. Current developments of SLM machines using multiple powerful laser beams to accelerate the fabrication process speed, adds to the demand for investigating the spatter formation during SLM fabrication.

In the present work, high-speed photography is utilized to realize the formation mechanisms and behavior of spatter particles during SLM fabrication. A computational image analysis framework is developed and applied to obtain the size and the number of induced spatters. Spatter distribution while two laser beams are working together is compared with the one laser operation condition. It is shown that using multi-laser technology significantly increases the number and the size of induced spatter particles. The morphology and the composition of spatters and their influence on the surface of the fabricated parts are also determined in this paper. The good agreement reported between the photography results and the microscopic examination of SLM parts reveals the facts that spatter detection using a high-speed camera is a reliable method if it is applied properly. The effect of spatter formation on failure mechanisms of SLM products are studied and a discussion is made on requirements for development of a systematic process parameter optimization to enhance the mechanical properties of SLM products.

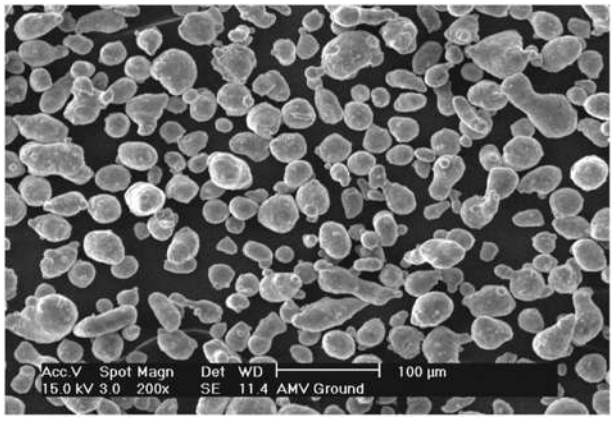

Fig. 2. Scanning Electron Microscopy (SEM) micrograph of the fresh Al-Si_{10}-Mg alloy powder. The average particle size is ranging between 30 µm to 50 µm.

2. Materials and methods

2.1. SLM process

An SLM 280HL (SLM Solutions Inc., Lübeck Germany) machine is used for SLM fabrication. The machine is equipped with two 400 W CW Ytterbium fiber lasers and a 280 mm × 280 mm × 350 mm building chamber. The beams are directly focused on two systems of galvanometric mirrors and have beam diameters of approximately 80 mm at the focal point of lasers radiation. Fig. 1 shows the sequences of operation of SLM 280HL machines schematically. First, the bi-directional recoating devices deposit the powder with a predefined thickness on the building platform from the left end (Fig. 1a) and stops at the right end. Then, the laser beam selectively melts the powder layer based on the geometrical information of the sliced computer aided design

Table 1
Process parameters and the resulting energy input used in this study.

Effective Laser Power W	Layer Thickness µm	Scan Velocity mm/s	Hatch Space µm	Energy Input J/mm^3
300	30	1650	120	50.5

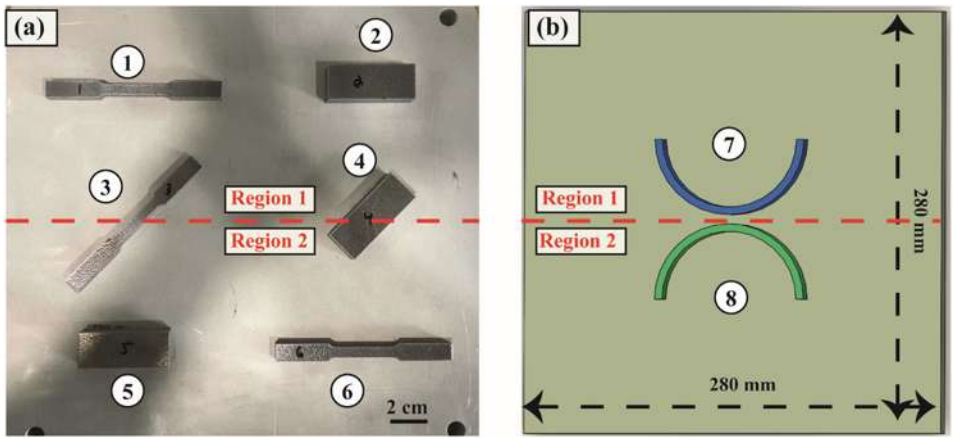

Fig. 3. Image/Schematic representation of samples fabricated by one/two laser beams. Region 1 and Region 2 indicate the working region of each laser. (a) Building platform of SLM 2800HL. Specimens 1, 2, 5, and 6 are made by one laser, and specimens 3 and 4 are made by two lasers. (b) Schematic representation of specimens used for taking high-speed video while two lasers are working close to each other.

(CAD) model (Fig. 1b). During laser processing, the powder heats up and becomes molten upon absorption of laser radiation. The molten powder particles bind to each other and re-solidify to produce a fully dense layer. After solidification, the building piston drops down to accommodate deposition of the next layer (Fig. 1c). Consequently, the laser beam starts fusing the next layer and in the meantime, the Powder Supply Unit (PSX) fills the recoating devices (Fig. 1d). This procedure is repeated several times until the final parts are created completely. The entire process is carried out under high purity argon gas to keep oxygen low in the building chamber during the fabrication process.

2.1.1. Materials and manufacturing conditions

The pre-alloyed gas atomized Al-Si10-Mg powder is used for SLM fabrication. As shown in the Scanning Electron Microscopy (SEM) micrograph of powder in Fig. 2, only a fraction of the powders had a spherical shape and most of the particles have prevalently irregular elongated shapes. The average spherical particle size is ranging between 30 μm and 50 μm.

The process parameters used in this work are described in Table 1. Since the laser power, scan velocity, layer thickness, and the hatch space are the most prominent factors in spatter creation

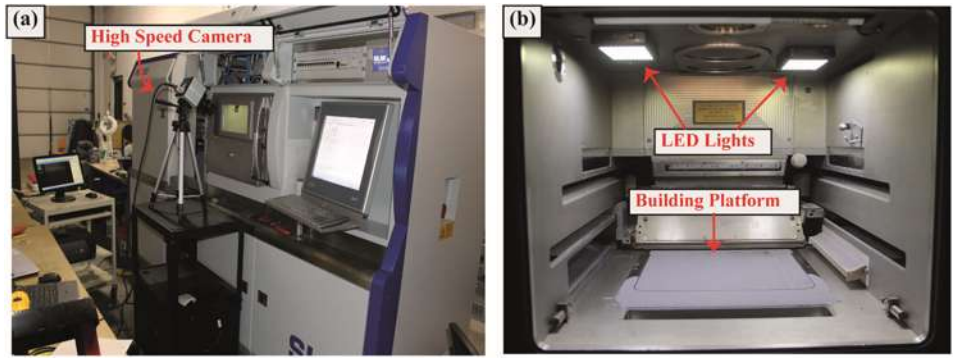

Fig. 4. A view of the experimental setup. (a) A high-speed camera is placed in front of 2800 SLM machine to capture the process. (b) SLM 280 HL building chamber. LED lights are placed inside of the chamber to provide enough light for high-speed video photography.

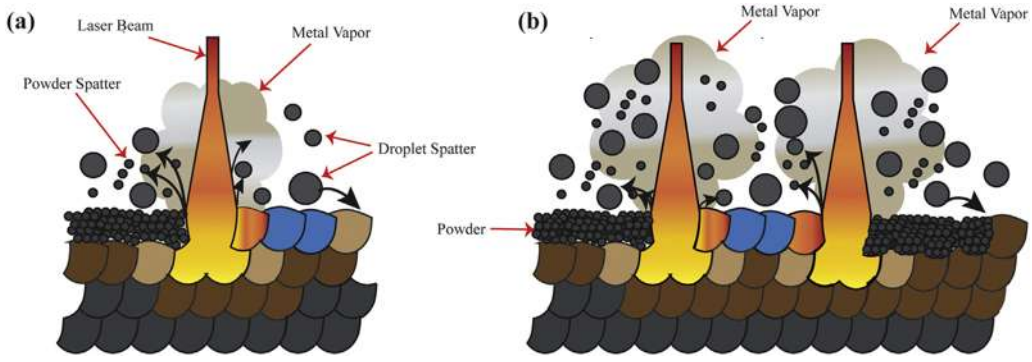

Fig. 5. Schematic representation of spatter creation during SLM process. (a) One laser beam is operating and the induced recoil pressure above the melting pool creates powder and droplet spatters. (b) Two laser beams are working closely and greater number of spatters are creating.

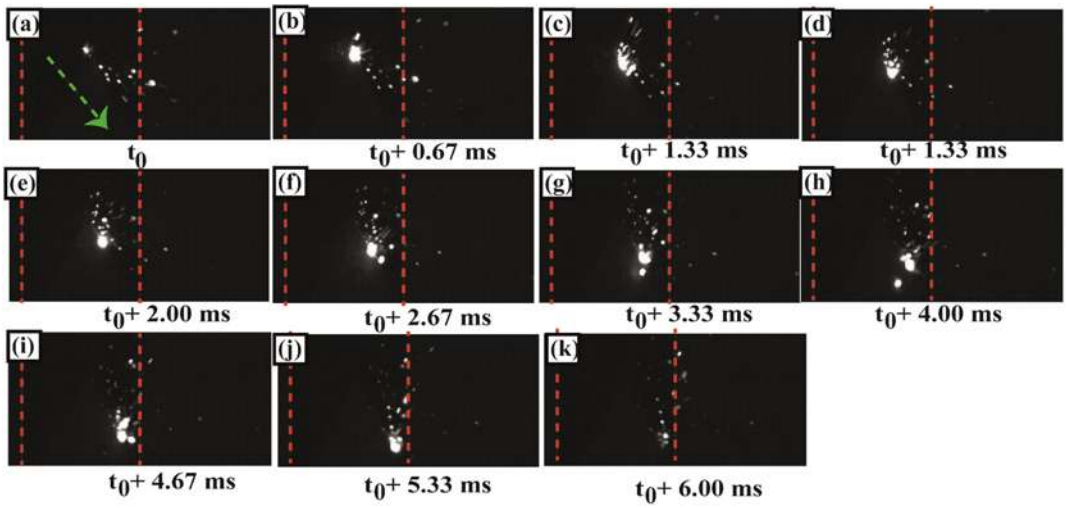

Fig. 6. High-speed camera images during one laser track in SLM process using one laser beam at a time. The time interval between each image is 0.67 milliseconds. The green arrow shows the laser track path and the dot red line shows the outline of the fabricated bulk specimen (see sample 3 in Fig. 3a). (For interpretation of the references to colour in this figure legend, the reader is referred to the web version of this article.)

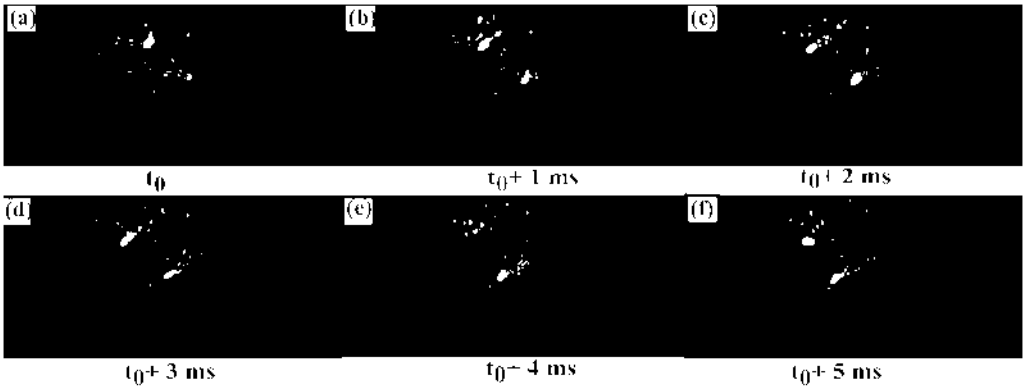

Fig. 7. High-speed camera images during SLM process while two laser beams are working closely. The time interval between each image is 1 millisecond. The red arrows show the laser track paths. The schematics of fabricated parts are shown in Fig. 3b. (For interpretation of the references to colour in this figure legend, the reader is referred to the web version of this article.)

mechanism, the energy input is calculated using the following relation [18]:

$$E = \frac{P}{v.h.t} \tag{1}$$

where P, v, h, and t are laser powder (W), laser scanning speed (mm/s), hatch spacing (mm), and layer thickness (mm), respectively.

Fig. 3 shows the schematic representation of samples made in this study. A dashed red line indicates the laser work area of each two-laser beam. Dense cuboid 10 mm × 6 mm × 10 mm samples are

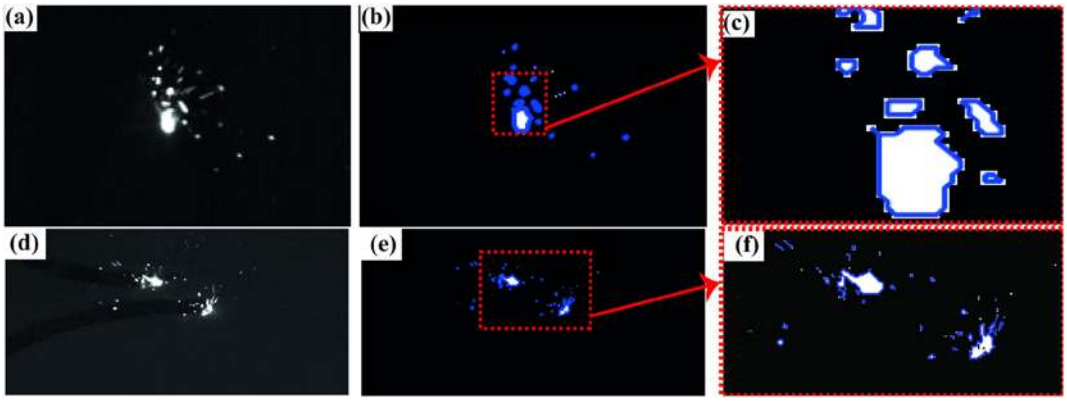

Fig. 8. Examples of high-speed camera image segmentations. (a) Actual recorded image during the SLM process while one laser is operating. (b) The segmented image of Fig. 8a. (c) High magnification of Fig. 8b close to the laser beam. (d) Actual recorded image during the SLM process while two lasers are operating close to each other. (e) The segmented image of Fig. 8d. (f) High magnification of Fig.8e close to the laser beams.

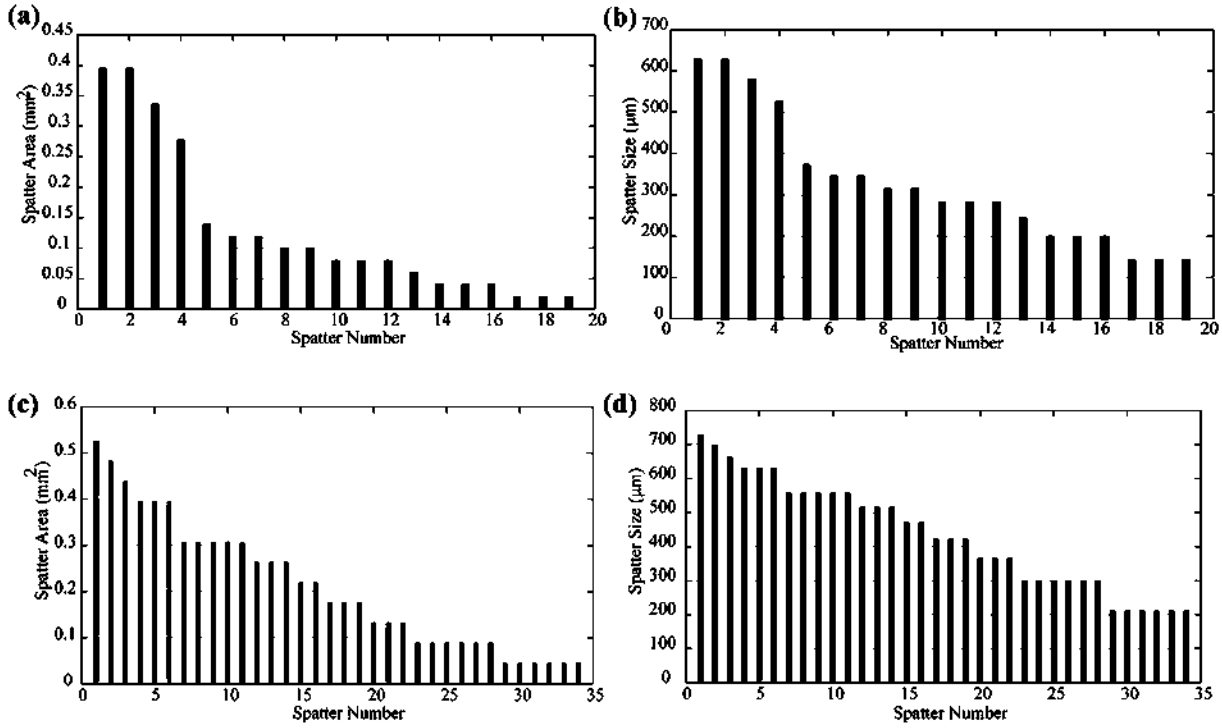

Fig. 9. Spatter distribution within an image frame using one laser beam (a, b) or two laser beams operating closely (c. d). (a) The area of the segmented spatters in an image frame shown in Fig. 8b. (b) The size (diameter) of the segmented spatters in an image frame shown in Fig. 8b. (c) The area of the segmented spatters in an image frame shown in Fig. 8e. (d) The size (diameter) of the segmented spatters in an image frame shown in Fig. 8d.

fabricated for density and microscopic analysis (see Fig. 3a). Tensile specimens are built in accordance with the ASTM/E8 standard [19] as shown in Fig. 3a. Two semicircular parts shown in Fig. 3b are designed to monitor the operation of two laser beams while they are working closely.

2.2. Material characterization methods

Microscopy analysis is performed by optical microscopy (Leica DM4000M) and by Scanning Electron Microscopy (SEM) (LEO1530VP). Cuboid samples are polished through several stages, using a finer paper (higher number) for each successive step. For polishing, diamond suspensions of 9 μm, 6 μm and 3 μm and finally, alumina suspensions of 1 μm and 0.05 μm are used to produce a smooth surface. The density is analyzed by means of the Archimedes principle (ASTM B962 – 14) on cuboids parts using Mettler balance (Type AE200) with a specific density measurement device for solid materials (Type AB33360). The chemical composition of the spatter particles is identified by Energy-dispersive X-ray Spectroscopy (EDS) analysis using an EDAX Genesis 4000 system. Tension tests are conducted by the 150 kN INSTRON machine. A strain rate of 10^{-4} s^{-1} is employed to failure. The strain is measured by an EPSILON extensometer with a gauge length of 25 mm which is attached to the samples. Tensile tests are repeated three times and their average response is plotted

2.3. High-speed photography

To capture the spatter mechanism/dynamics during laser processing, a high-speed camera (Fastcam 1024 PCI) is employed as shown in Fig. 4a. To prevent any light scattering in laser scanning process, the appropriate interference filter is placed in front of the camera lens. As shown in Fig. 4b, external light sources are utilized in the building chamber to provide enough light for capturing video at speeds of 6000 and 3000 frames per second (fps).

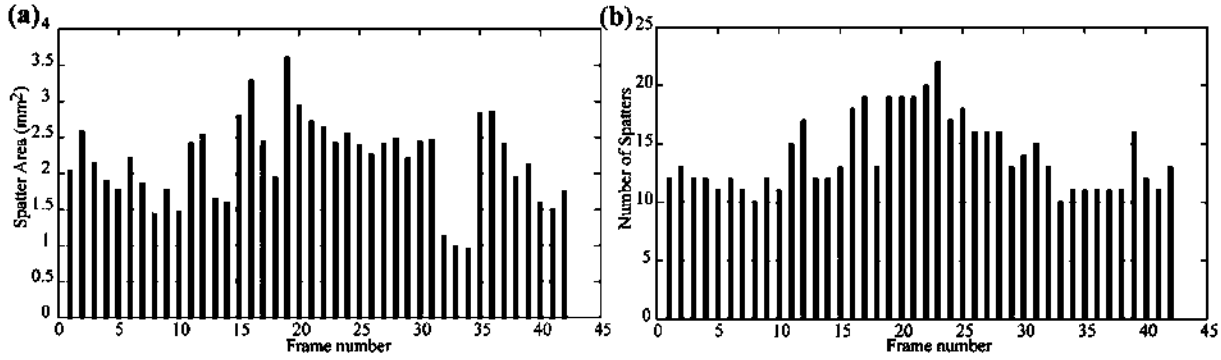

Fig. 10. Spatter distribution within the laser scan track (11.55 mm) while one laser beam is used. One laser scan track includes 42 image frames (each frame ~0.167 ms). (a) The total area of segmented spatter in each frame vs frame number. (b) Numbers of segmented spatters in each frame vs frame number.

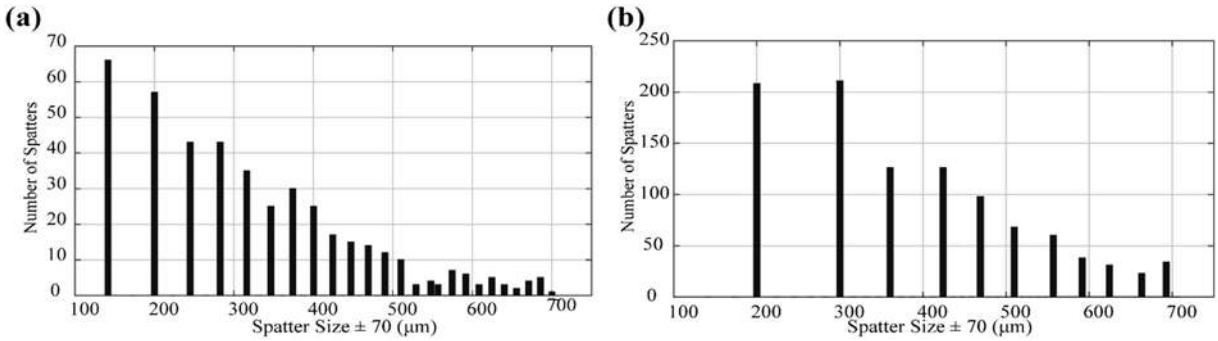

Fig. 11. Spatter size distribution within 144 milliseconds of laser(s) operation. (a) The number of segmented spatters in various spatter sizes (diameters) range while one laser is operating. (b) The number of segmented spatters in various spatter sizes (diameters) range while two lasers are operating closely (see Fig. 3b).

3. Results and discussion

3.1. Spatter creation mechanisms

High energy density of the focused laser beam during the SLM process causes the melt pools to reach the evaporation point of the material at the center of the laser spot. Consequently, a recoil pressure is made above the melting pool as shown in Fig. 5a. While low recoil pressure facilitates the flattening of the molten pools in SLM, high recoil pressure causes the molten material to be removed by melt expulsion [20,21]. The ejected metal is cooled down very quickly and condensates, forming particles with different particle sizes depending on the duration of the condensation process [22]. These particles are called droplet spatters in this paper. Furthermore, the strong influences of the laser plume dynamics on non-melted powder around the melting pool leads to eject the powder near the melt pool from the powder bed. These particles are called powder spatter in this paper. Both types of spatters are deposited into the unmelted powder or the solidified layer. As shown in Fig. 5b, by increasing the number of the operating laser beams, much greater amount of spatters are induced.

3.2. Spatter particles observation

High-speed camera images during a laser track, while one laser is operating at span of time during the manufacturing process (part 5 shown in Fig. 3a) are shown in Fig. 6. The laser track length and the operation time are 9.9 mm and 6 ms, respectively. It can be observed from Fig. 6a that there are several spatter particles left from the previous scan track. As the melting process started (Fig. 6a), the spatter particles are creating and dispersing around of the melting pool (Fig. 6b–j). The laser beam is then turned off (Fig. 6k) and the amount of induced spatters is reduced rapidly.

Fig. 7 shows the operation process of two laser beams while they are working close to each other (see Fig. 3b). The spatter particles are generating continuously during the fusion process. As shown in Fig. 6a and e, the number of the induced spatters is decreasing when one of the lasers is starting/finishing its own track and doesn't operate.

3.3. Spatter particles distribution assessment

To quantitate the number and the area of produced spatters, a custom-written MATLAB code is developed to analyze the high-speed

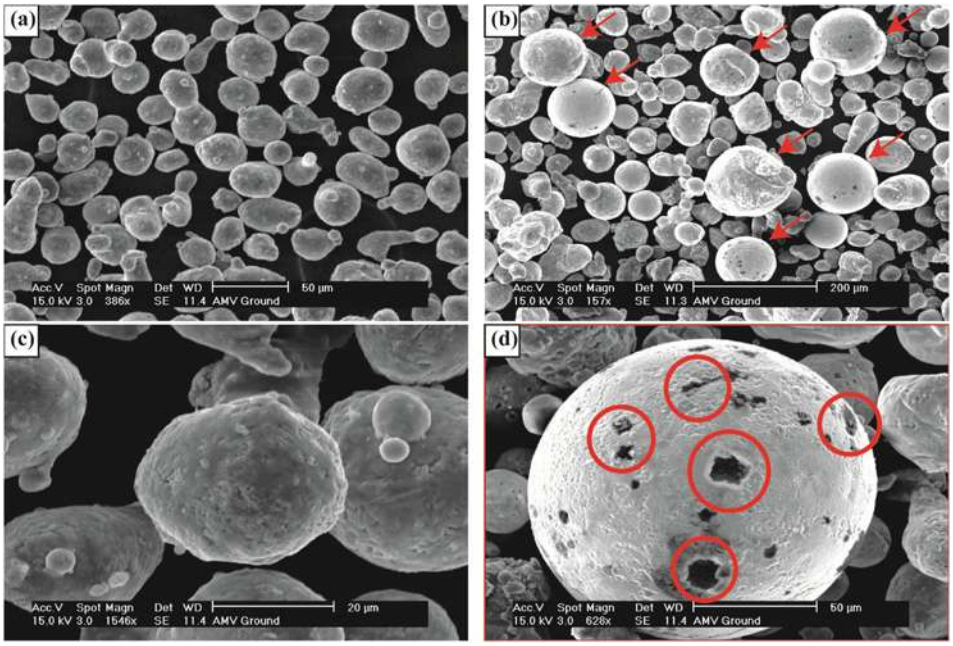

Fig. 12. SEM images of clean/dirty powders. (a) SEM micrograph of the fresh Al-Si10-Mg alloy powder before SLM process. The average size of particles is 30–50 μm and they have a spherical geometry. Scale bar = 50 μm (b) SEM micrograph of the powder after SLM process. The powder contains several spatters as shown by red arrows. Scale bar = 200 μm. (c) SEM micrograph of one particle with the size (diameter) of 35 μm. Scale bar = 20 μm (d) SEM micrograph of one spatter. The spatter size (diameter) is 200 μm. Scale bar = 500 μm. The spatter contains some black regions as indicated by red circles. The black region are representing the surface oxide due to a strong affinity of Mg to oxygen. (For interpretation of the references to colour in this figure legend, the reader is referred to the web version of this article.)

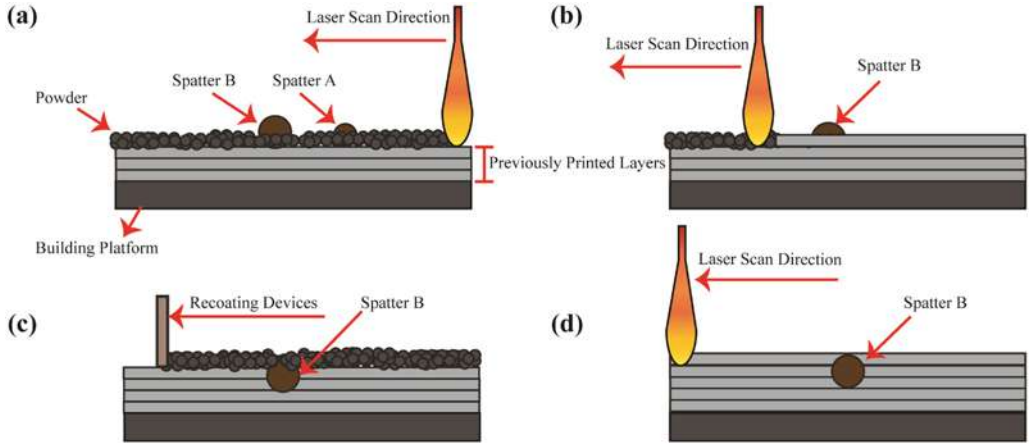

Fig. 13. Schematic representations of the inclusion creation mechanism by spatter particles mixed into the metallic powder during SLM process. (a) Spatter particles A and B are mixed with the metallic powder. (b) The laser melts the spatter A which has a particle size close to the layer thickness, but cannot melt the spatter B because of its size being much larger than the layer thickness. (c) New powder layer is deposited on the building platform. (d) Laser beam creates the next layer and the spatter B remains as an un-melted region in the final product.

camera images. Thresholding technique, using Otsu's method, is employed for image segmentation and a proper threshold constant is selected to detect the spatter boundaries correctly as shown in Fig. 8c and f. The details of Otsu's method is available elsewhere [23]. Fig. 8b and e show the processed images of the actual captured images shown in Fig. 8a and d, respectively.

Fig. 9a and b show the spatter distribution within the frame shown in Fig. 8a in which only one laser beam is operating. The number of detected spatters is nineteen and their corresponding areas and diameters are varied in the range of 0.02 mm^2–0.4 mm^2 and 120 μm–620 μm, respectively. Furthermore, spatter distributions within the frame shown in Fig. 8d are given in Fig. 9c and d. In this case, two lasers are operating together and the number of detected spatters is thirty-four. The diameter and the area of detected spatters are in the range of 200 μm–720 μm and 0.05 mm^2–0.52 mm^2, respectively. The difference between the number/size/area of the detected spatters in the case of one laser beam is operating and two laser beams working close together are in the good agreement with the described spatter creation mechanism in Section 3.1.

To quantify the spatter creation mechanism along one laser track, the fusion paths (shown in Fig. 6) are examined. The total number of created spatters and their corresponding area in each frame are shown in Fig. 10. The first and the last frames when the laser beam is not operating has the minimum numbers of created spatter. The greatest number of spatters corresponds to frames at the middle of the path. In these frames, the laser creates high enough recoil pressure to eject metallic material along with the powder spatters. As the laser reaches its end, the number of spatters are decreased, probably because the generated spatters in these frames as well as previous ones fall down to either powder bed or solidified layer very rapidly. The speed of spatter particles need to be studied in a future research. As it can be seen in Fig. 10, a variation of the total spatter area and the total number of spatter along the laser track does not follow the same trend. Spatters can agglomerate and aggregate to different orders of magnitude and geometries depending on their creation mechanisms (see Section 3.1).

To assess the spatter distribution within several laser tracks, a proper time interval between the processing frames is determined. Therefore, each spatter will not be counted more than once. Fig. 11a and b show the spatter distribution within 114 ms of one laser and multiple laser operation, respectively. As shown in Fig. 11 the number of induced spatters, particularly the large particles (spatter diameters between 400 μm–700 μm), is greater while two lasers are working compare to one laser beam operation condition. Higher induced recoil pressure by multiple laser beams and the position of solidified the yield the ejection of larger molten material from melting pools.

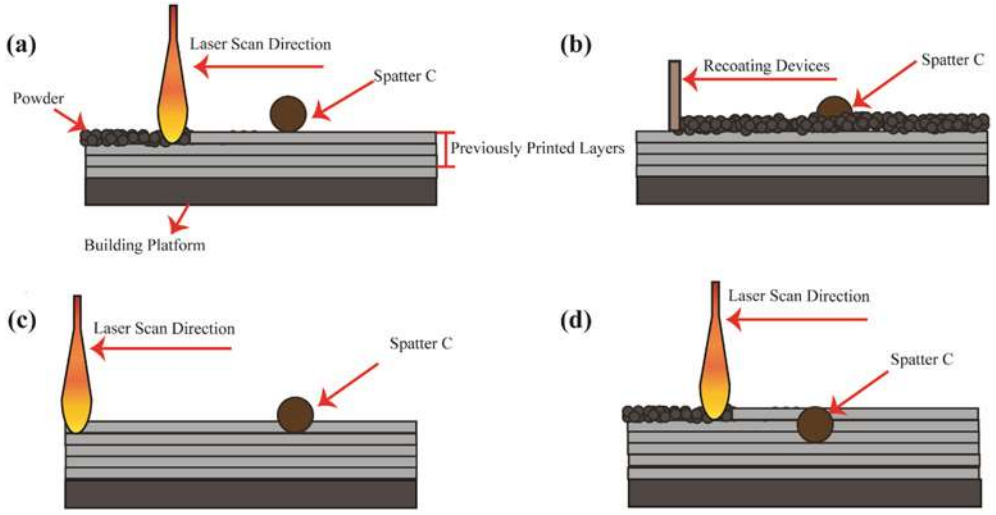

Fig. 14. Schematic representations of the inclusion creation mechanism by spatter particles which fall on the surface of solidified layers during SLM process. (a) Spatter particle C deposits on the last solidified layer. (b) New powder layer is deposited on the building platform while it cannot cover spatter C. (c) Laser beam creates the next layer and the spatter C stays on the build surface. (d) Next powder layer is deposited and while the laser beam creates the following layer, Spatter C remains as an unmelted region in the final product.

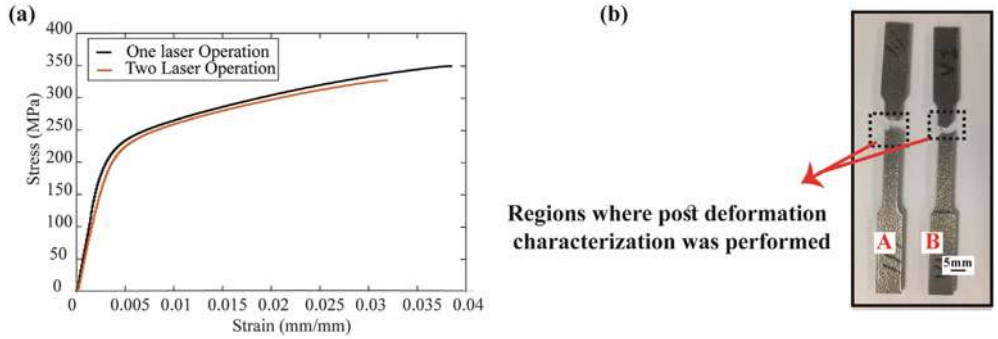

Fig. 15. (a) Representative engineering stress-strain curve of uniaxial tension samples made by one laser beam and two laser beams. The curves show the differences in strength and elongation values. (b) Images of tensile specimens made by one laser (B) and two laser beams (A) after failure.

3.4. Characterization of spatter particles morphology and their composition

The shielding gas flow which depending on its local velocity profile, may avoid depositing spatter particles on powders which are exposed to the laser beam afterward or in the layers just consolidated by the laser beam(s). However, due to the size of spatter particles (see Fig. 11), remarkable amount of spatters will fall onto the powder bed or solidified layers (see Fig. 5). Fig. 12a and b show the SEM photography of the powders before SLM process (called clean powder), and the collected metallic powders that have not laser melted after SLM process (called dirty powder), respectively. The particles sizes range between 30 μm and 50 μm for clean powder, and 30 μm to 200 μm for dirty powders. Fig. 12d shows the morphology of one of the Al-Si10-Mg laser spatters. The spatter is much larger than the clean powder particle (see Fig. 12c) and is mainly spherical. The spherical shape of the spatter is due to the fact that molten metal is solidifying before impinging on the powder bed. Fig. 12d also shows that the surface of the spatter contains dark patches (marked with red circle), suggesting a difference in chemical composition. The EDS analysis reveals that these areas are surface oxides. This is because Mg alloy elements, due to their high affinity to oxygen, react with the remaining oxygen in the building chamber during flight process. These findings are in agreement with other studies on the spatter compositions [15].

3.5. Effect of spatter particle creation on As-built SLM components

Fig. 13a shows the schematic illustration of the spatter particles mixed with the metallic powder which is exposed to the laser beam afterward. Depending on the size of spatter particles (see Fig. 9), the melting point of the material, and the amount of energy input of the beam, the laser beam may or may not melt the spatter particles during SLM process (see Fig. 13b). As shown in Fig. 13a, the size of spatter A is close to the powder layer thickness and it can be completely melted by the laser beam as shown in Fig. 13b. However, since the size of the spatter B is larger than the powder layer thickness, the laser cannot melt it (see Fig. 13.b) and as the next layer is formed (Fig. 13.c and d), the spatter particle B creates an inclusion in the part.

A similar trend can be observed when the spatter particles fall into the layers which are just consolidated by the laser beam(s). Fig. 14a shows a representative spatter called “Spatter C” which is redeposited on the surface of the solidified layers. As the recoating devices drag powder across the build surface (Fig. 14b) and laser beam melts the next layer, the spatter C is not melted and stays on the build surface (Fig. 14c). Subsequently, a new powder layer is coated on the build surface and while the laser beam creates the next layer, the spatter remains as a non-melted region into the part (Fig. 14d).

These unmelted regions and inclusions are the major sources of crack initiation during tensile loading. Fig. 15a shows the typical engineering stress-strain curves for the specimens made by one laser (Part B shown in Fig.15b) and two laser beams (Part A is shown in Fig. 15b). Average strength and fracture values for these parts are given in Table 2. The results show that specimens fabricated by two lasers have lower strength and ductility, compared to the samples made by one laser beam. As mentioned previously, the number and the corresponding size of induced spatters are greater while multi-laser beams are working together, compare to one laser operation condition. Consequently, the total induced inclusions in sample A (Fig.15b) is greater than sample B (Fig. 15b), which decrease the strength of the final product.

Fig.16 shows the fracture surface of specimens made by one laser beam. The existence of dimples are representative of a ductile fracture. It worth noting that un-melted regions and inclusion (close to the surface of specimens) are reported as stress risers, and serve as main sites of crack initiation for specimens failed in high cyclic fatigue [24]. This is mainly because the influence of defects on fatigue life is more prominent in the high cycle fatigue regime, in which crack initiation constitutes a dominant part of total fatigue life.

Fig. 17a and b show the optical micrographs of the surface of SLM samples made by one laser (Sample 2 shown in Fig. 3a) and two laser beams (Sample 4 shown in Fig. 3a), respectively. The figures indicate that the size of inclusions created on the surface of SLM part while one laser beam operated and multiple lasers worked together are varied between 20 and 200 μm and 20–560 μm, respectively. There are several factors during the SLM process which can result in creation of porosities and inclusions. However, since the current process parameters are optimized to provide almost a fully dense part (Table 3), the most portion of the detected inclusion on the SLM parts, are related to spatter particles deposition. Indeed, these observations are in good consent with high-speed camera image detections shown in Fig. 11.

Table 3 shows the relative density of the parts made by both one laser (Sample 2 shown in Fig. 3a) and two laser beams (Sample 4 shown in Fig. 3a). The results demonstrate that the unmelted regions or inclusions created by spatters have not significantly affected the density of final products. However, as it is explained above, they have remarkable influence on the mechanical properties, especially fatigue resistance of parts. Consequently, it can be concluded that optimizing the AM process parameters for maximum part density using Archimedes' principle is not a sufficient means to achieve an SLM part with an

Table 2
Summary of mechanical properties measured in this work. Sample made by one laser beam shows higher strength and ductility, compared to the samples made by two beams.

Type	Yield Stress MPa	Fracture Stress MPa	Fracture Strain %
Sample made by one laser beam	215	350	3.85
Sample made by two laser beams	211	327	3.18

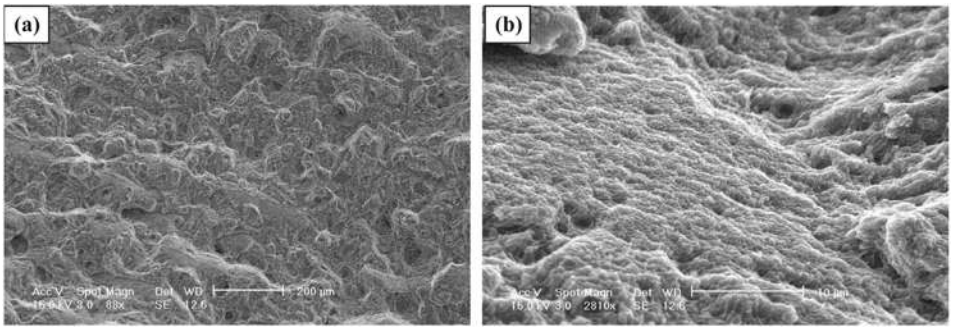

Fig. 16. Fractography of the sample made by one laser beam (Fig. 15b-B). (a) There are some pores in the fracture surface acts as cracks initiators. (b)The specimens have ductile fracture due to the existence of dimples in the fracture surface.

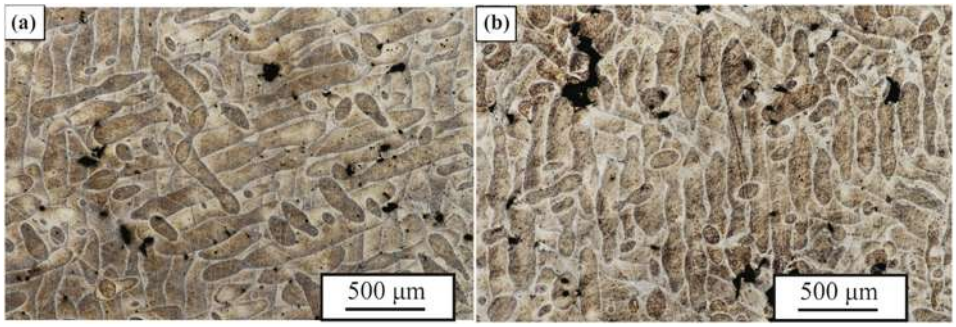

Fig. 17. Optical micrographs of etched surfaces of the SLM parts fabricated by (a) one laser beam, and (b) two laser beams.

acceptable mechanical property (especially fatigue strength). Further researches are needed to identify factors related to spatter creations in SLM products for optimizing SLM manufacturing process conditions.

4. Conclusions

The spatter creation mechanisms during selective laser melting (SLM) with multi-laser technology are investigated. The dynamic processes of spatter behavior are recorded using a high-speed camera. The spatters sizes and their distribution obtained by different conditions, including the number of operating lasers, are assessed. The number of operating laser beams significantly influences the spatter creation mechanisms during SLM process. A higher number of working laser beams induces greater recoil pressure above the melting pools and ejects a larger amount of metallic material from molten pools. It is shown that spatter particles size is much larger than the starting pre-alloyed powders. The particle shape of spatter is mainly spherical. EDS analyses show the surface of spatter contains oxygen due to a strong affinity of Mg to oxygen. Analyzing the tensile testing results indicates that although both groups of specimens made by one- and multi-laser beams are characterized by ductile fracture, the tensile properties of samples manufactured by one laser beam are greater than those made by multi-laser beams. This phenomenon can be attributed to the larger amount of induced inclusions in multi-laser beam method. Finally, based on the density analysis, it is concluded that optimization of manufacturing process parameters by maximizing the scalar density is not a sufficient means to enhance the mechanical properties (especially fatigue strength) of SLM products. More attention needs to be paid for finding and developing optimization methods to generate parts with minimum unmelted regions induced by spatter particles, which consequently improves the mechanical properties.

Table 3
Mean densities of the parts made by one or two laser beams. Densities are obtained by Archimedes' principle using ASTM B962–14 (Density of water = 0.9978, Density of Air = 0.001225).

Type	m_{air}	m_{fluid}	Density	Relative Density
Sample made by one laser beam	0.7711	0.4834	2.6722	99.7114
Sample made by two laser beams	0.6596	0.4094	2.6284	98.0778

Acknowledgment

The authors would like to acknowledge Dr. Richard Grylls, Kyle Adams, and Michael Hansen from SLM Solutions Inc. for helping the authors to conduct the experiments.

Appendix A. Supplementary data

Supplementary data to this article can be found online at http://dx.doi.org/10.1016/j.matdes.2017.06.040.

References

[1] I. Gibson, D.W. Rosen, B. Stucker, Additive Manufacturing Technologies, Springer, 2010.
[2] A.T. Clare, P.R. Chalker, S. Davies, C.J. Sutcliffe, S. Tsopanos, Selective laser melting of high aspect ratio 3D nickel–titanium structures two way trained for MEMS applications, Int. J. Mech. Mater. Des. 4 (2) (2008) 181–187.
[3] B. Berman, 3-D printing: the new industrial revolution, Bus. Horiz. 55 (2) (2012) 155–162.
[4] M. Elahinia, N.S. Moghaddam, M.T. Andani, A. Amerinatanzi, B.A. Bimber, R.F. Hamilton, Fabrication of NiTi through additive manufacturing: a review, Prog. Mater. Sci. 83 (2016) 630–663.
[5] W.E. Frazier, Metal additive manufacturing: a review, J. Mater. Eng. Perform. 23 (6) (2014) 1917–1928.
[6] V. Weißmann, R. Bader, H. Hansmann, N. Laufer, Influence of the structural orientation on the mechanical properties of selective laser melted Ti6Al4V open-porous scaffolds, Mater. Des. 95 (2016) 188–197.
[7] M. Leary, M. Mazur, J. Elambasseril, M. McMillan, T. Chirent, Y. Sun, M. Qian, M. Easton, M. Brandt, Selective laser melting (SLM) of $AlSi_{12}Mg$ lattice structures, Mater. Des. 98 (2016) 344–357.
[8] J.M. Walker, C. Haberland, M. Taheri Andani, H.E. Karaca, D. Dean, M. Elahinia, Process development and characterization of additively manufactured nickel–

titanium shape memory parts, J. Intell. Mater. Syst. Struct. 27 (19) (2016) 2653–2660.
[9] M. Taheri Andani, Modeling, Simulation, Additive Manufacturing, and Experimental Evaluation of Solid and Porous NiTi, University of Toledo, 2015.
[10] Anon, 3D Printing and the New Shape of Industrial Manufacturing, Del. PricewaterhouseCoopers LLP, June 2014 1e9.
[11] D. Low, L. Li, A. Corfe, Characteristics of spatter formation under the effects of different laser parameters during laser drilling, J. Mater. Process. Technol. 118 (1) (2001) 179–186.
[12] D. Low, L. Li, P. Byrd, Spatter prevention during the laser drilling of selected aerospace materials, J. Mater. Process. Technol. 139 (1–3) (2003) 71–76.
[13] L.E. Criales, Y.M. Arısoy, B. Lane, S. Moylan, A. Donmez, T. Özel, Laser powder bed fusion of nickel alloy 625: experimental investigations of effects of process parameters on melt pool size and shape with spatter analysis, Int. J. Mach. Tools Manuf. (2017).
[14] S.A. Khairallah, A.T. Anderson, A. Rubenchik, W.E. King, Laser powder-bed fusion additive manufacturing: physics of complex melt flow and formation mechanisms of pores, spatter, and denudation zones, Acta Mater. 108 (2016) 36–45.
[15] M. Simonelli, C. Tuck, N.T. Aboulkhair, I. Maskery, I. Ashcroft, R.D. Wildman, R. Hague, A study on the laser spatter and the oxidation reactions during selective laser melting of 316L stainless steel, Al-Si_{10}-Mg, and Ti-6Al-4V, Metall. Mater. Trans. A 46 (9) (2015) 3842–3851.
[16] K. Mumtaz, N. Hopkinson, Selective laser melting of thin wall parts using pulse shaping, J. Mater. Process. Technol. 210 (2) (2010) 279–287.
[17] Y. Liu, Y. Yang, S. Mai, D. Wang, C. Song, Investigation into spatter behavior during selective laser melting of AISI 316L stainless steel powder, Mater. Des. 87 (2015) 797–806.
[18] M.T. Andani, C. Haberland, J. Walker, M. Elahinia, An Investigation of Effective Process Parameters on Phase Transformation Temperature of Nitinol Manufactured by Selective Laser Melting, ASME 2014 Conference on Smart Materials, Adaptive Structures and Intelligent Systems, American Society of Mechanical Engineers, 2014 (pp. V001T01A026–V001T01A026).
[19] A. Standard, E8, Standard Test Methods for Tension Testing of Metallic Materials, Annual Book of ASTM Standards, 3, 2004 57–72.
[20] R. Fabbro, M. Hamadou, F. Coste, Metallic vapor ejection effect on melt pool dynamics in deep penetration laser welding, J. Laser Appl. 16 (1) (2004) 16–19.
[21] R. Fabbro, S. Slimani, I. Doudet, F. Coste, F. Briand, Experimental study of the dynamical coupling between the induced vapour plume and the melt pool for Nd–Yag CW laser welding, J. Phys. D. Appl. Phys. 39 (2) (2006) 394.
[22] A. Ladewig, G. Schlick, M. Fisser, V. Schulze, U. Glatzel, Influence of the shielding gas flow on the removal of process by-products in the selective laser melting process, Addit. Manuf. 10 (2016) 1–9.
[23] N. Otsu, A threshold selection method from gray-level histograms, Automatica 11 (285–296) (1975) 23–27.
[24] A. Yadollahi, N. Shamsaei, S.M. Thompson, A. Elwany, L. Bian, Effects of building orientation and heat treatment on fatigue behavior of selective laser melted 17-4 PH stainless steel, Int. J. Fatigue (2016).